Structure and dynamics of the supercluster of galaxies SC0028-0005

Ana Laura O'Mill,[1,2]★ Dominique Proust,[3] Hugo V. Capelato,[4,5] Mirian Castejon,[1] Eduardo S. Cypriano,[1] Gastão B. Lima Neto[1] and Laerte Sodré Jr[1]

[1]*Departamento de Astronomia, Instituto de Astronomia, Geofísica e Ciências Atmosféricas da USP, Rua do Matão 1226, Cidade Universitária, 05508-090 São Paulo, Brazil*
[2]*Instituto de Astronomía Teórica y Experimental, CONICET-UNC, Laprida 922, X5000BGR Córdoba, Argentina*
[3]*Observatoire de Paris-Meudon, GEPI, F-92195 Meudon, France*
[4]*Divisão de Astrofísica, INPE/MCT, 12227-010 São José dos Campos, São Paulo, Brazil*
[5]*Núcleo de Astrofísica Teórica, Universidade Cruzeiro do Sul, Rua Galvão Bueno, 868, CEP 01506-000 São Paulo, Brazil*

ABSTRACT

According to the standard cosmological scenario, superclusters are objects that have just passed the turn-around point and are collapsing. The dynamics of very few superclusters have been analysed up to now. In this paper, we study the supercluster SC0028-0005, at redshift 0.22, identify the most prominent groups and/or clusters that make up the supercluster, and investigate the dynamic state of this structure. For the membership identification, we have used photometric and spectroscopic data from Sloan Digital Sky Survey Data Release 10, finding six main structures in a flat spatial distribution. We have also used a deep multiband observation with MegaCam/Canada–France–Hawaii Telescope to estimate de mass distribution through the weak-lensing effect. For the dynamical analysis, we have determined the relative distances along the line of sight within the supercluster using the Fundamental Plane of early-type galaxies. Finally, we have computed the peculiar velocities of each of the main structures. The 3D distribution suggests that SC0028-005 is indeed a collapsing supercluster, supporting the formation scenario of these structures. Using the spherical collapse model, we estimate that the mass within $r = 10$ Mpc should lie between 4 and 16×10^{15} M$_\odot$. The farthest detected members of the supercluster suggest that within ~ 60 Mpc the density contrast is $\delta \sim 3$ with respect to the critical density at $z = 0.22$, implying a total mass of ~ 4.6–16×10^{17} M$_\odot$, most of which in the form of low-mass galaxy groups or smaller substructures.

Key words: galaxies: clusters: general – galaxies: kinematics and dynamics – cosmology: theory.

1 INTRODUCTION

In the hierarchical paradigm of structure formation, the smallest structures are the first to collapse and virialize. They later get collected into progressively larger structures, each of which goes through the same stages of collapse and virialization. At present, the largest collapsed structures are clusters of galaxies, whereas superclusters are expected to be in the stage of gravitational collapse, at least in their inner tens of Mpc (Reisenegger et al. 2000; Batiste & Batuski 2013; Merluzzi et al. 2015). In the currently favoured cosmological scenario, dominated by a cosmological constant or another form of 'dark energy', superclusters are starting to recede from each other at an accelerated rate, which will not allow them to get collected into even larger structures. Therefore, they are the largest structures that will ever collapse and virialize

(e.g. Busha et al. 2003; Nagamine & Loeb 2003; Dünner et al. 2006, 2007; Proust et al. 2006; Rines et al. 2013). If this scenario is correct, present superclusters play a pivotal role in our understanding of the evolution of the universe. Thus, it is very important to determine their quantitative properties such as masses, sizes, and densities reliably, as well as testing this scenario as best as possible. Since superclusters have not yet collapsed and virialized, they do not stand out against the background density field as clearly as individual galaxies or even clusters of galaxies (in terms of mass, optical light or X-ray emission), and equilibrium techniques used to determine the masses of clusters (hydrostatic equilibrium of the gas and virial equilibrium of the galaxies) do not apply to them.

The study of superclusters has a long history, beginning with works such as the identification of our own Virgo supercluster (de Vaucouleurs 1953) and the statistical description of 'clustering of second order' (which are known nowadays as the superclusters; Neyman, Scott & Shane 1956). Other studies addressed the

★ E-mail: anaomill@gmail.com

identification, distribution and characterization of these objects (e.g. Jõeveer, Einasto & Tago 1978; Einasto et al. 1984, 1994; Tago, Einasto & Saar 1984; Zucca et al. 1993), establishing that they are separated by large voids and clusters inside them are usually organized in chain-like structures.

Some studies considered the morphology of superclusters, based on the spatial distribution of their galaxies. Einasto et al. (2007, 2011) analysed a sample drawn from Sloan Digital Sky Survey Data Release 7 (SDSS-DR7), finding two main morphological types: filaments and others with a more complex, multibranch fine structure. The wide morphological variety of superclusters let Einasto et al. (2011) to suggest that their evolution have been dissimilar. Costa-Duarte, Sodré & Durret (2011) used a kernel-based density field method to identify the superclusters and Minkowski Functionals to quantify their shape. They found that filaments and pancakes represent distinct morphological classes of superclusters in the Universe. The filaments tend to be richer, more luminous and larger than pancakes. It is then plausible to think that pancakes evolve towards filaments.

While there is plenty of morphological analysis, dynamical studies of galaxy superclusters are more scarce. In the hierarchical model of structure formation we expect that galaxy clusters form through accretion of galaxies and groups or merger with other clusters in the environment of superclusters. In the case of a supercluster with several clusters, it is possible that massive clusters grow through the gravitational collapse of the central parts of superclusters. Therefore, superclusters are still far from equilibrium today. The collapse scenario predicts that, among the clusters in a supercluster, those with higher observed redshifts are falling in to the centre from the front side (and thus are closer to us), while those with lower observed redshifts are falling in from the back (and are therefore more distant). Consequently, in the gravitationally collapsing region, the Hubble relation is reversed. This effect is indeed present in the core of the Shapley Supercluster (Proust et al. 2006; Ragone et al. 2006; Dünner et al. 2007), at $z \simeq 0.04$. Batiste & Batuski (2013) made a dynamical analysis of the Corona Borealis supercluster at $z \simeq 0.07$ using data from the SDSS. They find this supercluster has broken from the Hubble flow and, based on dynamical simulations, conclude that a significant fraction of mass should reside outside the clusters comprising the supercluster. Recently, Tully et al. (2014) have used peculiar velocities to identify and describe a large and massive structure, Laniakea, comprising most of the galaxies in the local universe.

The picture of gravitationally collapsing central parts of superclusters is required by the present cosmological model, but it has been tested only at low redshifts. Indeed, previous dynamical studies, as those described above and in Section 5, dealt with superclusters below $z = 0.1$. In this work, we analyse the supercluster SC0028-0005, at $z = 0.22$, in order to test the collapse scenario for structures at intermediate redshift. This paper is organized as follows. In Section 2, we describe what is known about this supercluster and what is the data that we will analyse in this paper. In Section 3, we present an identification of the supercluster members. Section 4 contains a weak-lensing analysis of the substructures found in the supercluster. In Section 5, we show that the dynamical behaviour of the supercluster components is consistent with a collapsing scenario. For this analysis, we use the Fundamental Plane (FP) of early-type galaxies to obtain relative distances and peculiar velocities of these components. Finally, our results are summarized in Section 6. Throughout this paper we adopt, when necessary, a Λ cold dark matter (ΛCDM) cosmological model with $\Omega_M = 0.30$, $\Omega_\Lambda = 0.70$ and $H_0 = 70 \, h_{70} \, \text{km s}^{-1} \, \text{Mpc}^{-1}$.

Table 1. CFHT Imaging characteristics.

Band	Exposure (h)	Seeing (arcsec)	Completness (AB mag)
g	1.5	0.52	24.5
r	3.3	0.45	24.6
i	2.5	0.45	24.3

2 THE SUPERCLUSTER SC0028-0005

In this study, we focus on the galaxy supercluster SC0028-0005 (hereafter SC0028 for simplicity) at $\alpha = 00^h28^m$ and $\delta = -00°05'$ (J2000.0). It is in the catalogue of Basilakos (2003), obtained from the Sloan Digital Sky Survey (SDSS) 'Cut & Enhance' cluster catalogue (Goto et al. 2002) by applying a percolation radius $R_{pc} = 26 \, h^{-1}$ Mpc. Among the 57 superclusters of this catalogue, SC0028 is the number 38, with an assigned redshift $z = 0.197$, and is classified as a *filament* by using the shape finder estimator of Basilakos (2003). This structure was chosen for this study because it was not too complex in the Goto et al. (2002) catalogue, containing only three galaxy clusters with relative distances of 4–$10 \, h^{-1}$ Mpc between them, what was suggestive of the presence of strong peculiar motions.

2.1 Spectroscopic and photometric samples

We selected from the Data Release 10 of Sloan Digital Sky Survey[1] (SDSS-DR10) a sample of galaxies with spectroscopic and photometric data within an area of radius $1°.2$, centred on the supercluster.

SDSS DR10 covers an additional 3100 deg² of sky over the previous release and includes spectra obtained with the new spectrographs APOGEE and BOSS, whose sky coverage includes the region of SC0028.

The spectroscopic and photometric data sets were extracted from the `SpecObjAll` and `PhotoObj` tables of the `CasJobs`[2] data base. From the `PhotoObj` table we downloaded the `objID`, the coordinates, the model g and r magnitudes, the Galaxy extinction values, the effective radii derived from the de Vaucouleurs profile fit, as well as model magnitudes and axial ratios of the de Vaucouleurs fits, and the photometric redshifts. From the `SpecObjAll` table, we downloaded the spectroscopic redshifts and the galaxy central velocity dispersions plus the respective errors.

From this data, we selected two galaxy samples. The first sample comprises 4921 galaxies with spectroscopic redshift. This sample is employed to identify the supercluster members and substructures, as well as in the dynamical analysis of Section 5.

The second sample contains 35 757 galaxies with photometric redshifts (including the galaxies of the previous spectral sample), selected from the `PhotoObj` table. This sample allowed an analysis of the photometric properties of the substructures identified spectroscopically and is also useful for their detection.

2.2 CFHT Imaging

The supercluster field was observed with Canada–France–Hawaii Telescope (CFHT)/MegaCam in imaging mode, mostly for the weak-lensing analysis described in Section 4. We got deep, good quality g, r, i images, whose main features are shown in Table 1.

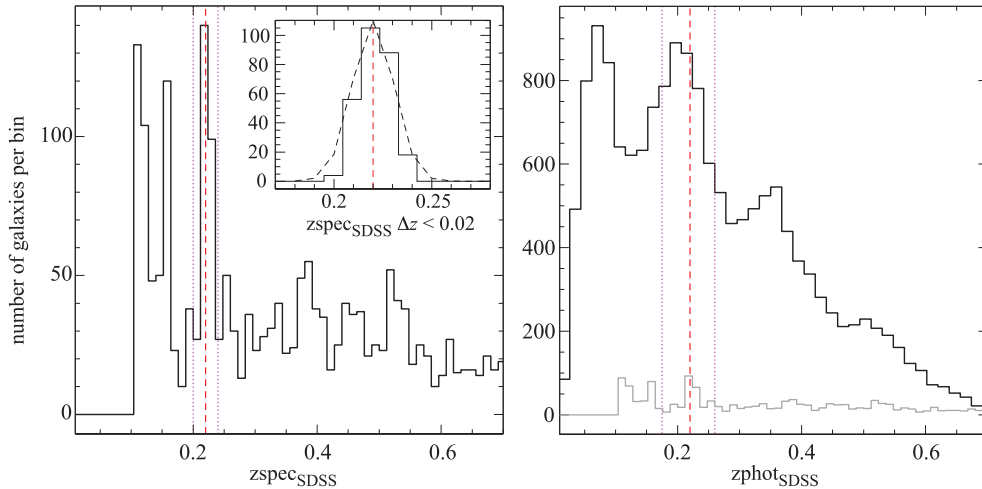[1] https://www.sdss3.org/dr10/
[2] http://skyserver.sdss3.org/CasJobs/

Figure 1. Redshift distribution within an area of 1°.2 radius centred on SC0028. Left-hand panel: spectroscopic redshift distribution. The inset shows the redshift distribution of galaxies in the $\Delta z < 0.02$ interval around the supercluster mean redshift, as well as a Gaussian fit of this distribution. Right-hand panel: photometric redshifts. The grey histogram correspond to the redshift sample, reported here for easy comparison. In both panels, the dashed vertical lines correspond to the supercluster mean redshift and the magenta dotted lines show the galaxies within a redshift interval around the mean of $\Delta z < 0.02$ for the S1 sample and $\Delta z_{phot} < 0.04$ for the S2 sample.

The whole data processing (bias and overscan subtraction, flat-fielding and sky subtraction), image combination and catalogue extraction with SEXTRACTOR (Bertin & Arnouts 1996) has been done by the Terapix[3] team, using the procedures described in Bertin et al. (2002).

The total integrations were obtained with a series of ~10 min exposures per filter, with small position offsets, for the coverage of the cap between the camera CCDs. As a result, the final combined image in each band covers an area slightly smaller than 1 deg² (MegaCam's full field of view).

3 IDENTIFYING THE SUPERCLUSTER MEMBERS

3.1 Selecting galaxies

With the aim of selecting galaxies which are members of the supercluster, we start by defining Δz as the absolute difference between a given redshift and the supercluster mean redshift. For galaxies with spectroscopic redshifts we consider as members those with $\Delta z < 0.02$. We call this sample S1. For those with photometric redshifts only, due to the larger uncertainties, we adopted $\Delta z_{phot} < 0.04$ (about twice the SDSS photometric redshift standard deviation). This we call the S2 sample.

Left- and right-hand panels of Fig. 1 show the resulting redshift distribution of the galaxies in the spectroscopic and photometric samples (Section 2.1), respectively. The peak around $z \simeq 0.22$ in these figures corresponds to the supercluster.

We selected galaxies from the spectroscopic sample which are supercluster members using the following approach. We pre-selected all galaxies in the range $0.195 < z < 0.245$, a redshift interval large enough to not exclude possible members, and small enough to avoid most fore/background galaxies. We fitted a Gaussian to the resulting redshift distribution, obtaining an average redshift of $\bar{z} = 0.220 \pm 0.001$. Around this value we selected the spectroscopic

sample, S1, using $\Delta z < 0.02$, resulting in a total of 271 galaxies. For the photometric sample we adopted $\Delta z_{phot} < 0.04$, obtaining 3549 galaxies. In both panels of Fig. 1 the magenta dotted lines bracket the membership ranges.

3.2 Identifying substructures

In order to identify substructures in our spectroscopic sample, we present a density map of the S1 sample in the upper-left panel of Fig. 2. This map was made by counting the number of galaxies in equal size square cells with 15 arcsec on a side. We found nine well-defined peaks in this density distribution which are most likely galaxy groups or clusters candidate members of SC0028. The brightest galaxy in each peak was taken as the group/cluster centre, and all galaxies in the sample within a 2.5 h_{70}^{-1} Mpc radius (~11.7 arcmin) of this centre were considered as group/cluster members. In this panel, the circles show the region around each peak ascribed to a certain group or cluster. Table 2 presents the identification, coordinates and mean redshift of each of these substructures. Note that they may be groups or galaxy clusters, but hereafter we will call them substructures.

The upper-right panel of Fig. 2 is similar to the left-hand panel, but uses the larger S2 sample (the photometric one) instead of the S1 sample.

The light map (Fig. 2, lower-left panel) was made by strongly smoothing the S2 sample of galaxies by a bidimensional Gaussian with intensity proportional to the galaxy luminosity and width proportional to their half-luminosity radius, $\sigma = 100R_{50}$. In this way, we can take into account the different apparent sizes of the galaxies. This luminosity field was then binned in a 2D grid with 15×15 arcsec² cells, producing an image. Since the mean R_{50} is ~1.1 arcsec, the typical galaxy luminosity was spread in a radius of ~7 pixel (1σ), which we found adequate to describe the substructures in the light distribution. This map is in qualitative agreement with the S1 density map, as there are peaks in most regions previously identified (solid line circles in Fig. 2).

The bottom-right panel of Fig. 2 shows the weak-lensing recovered projected mass distribution (see Section 4). The same structures
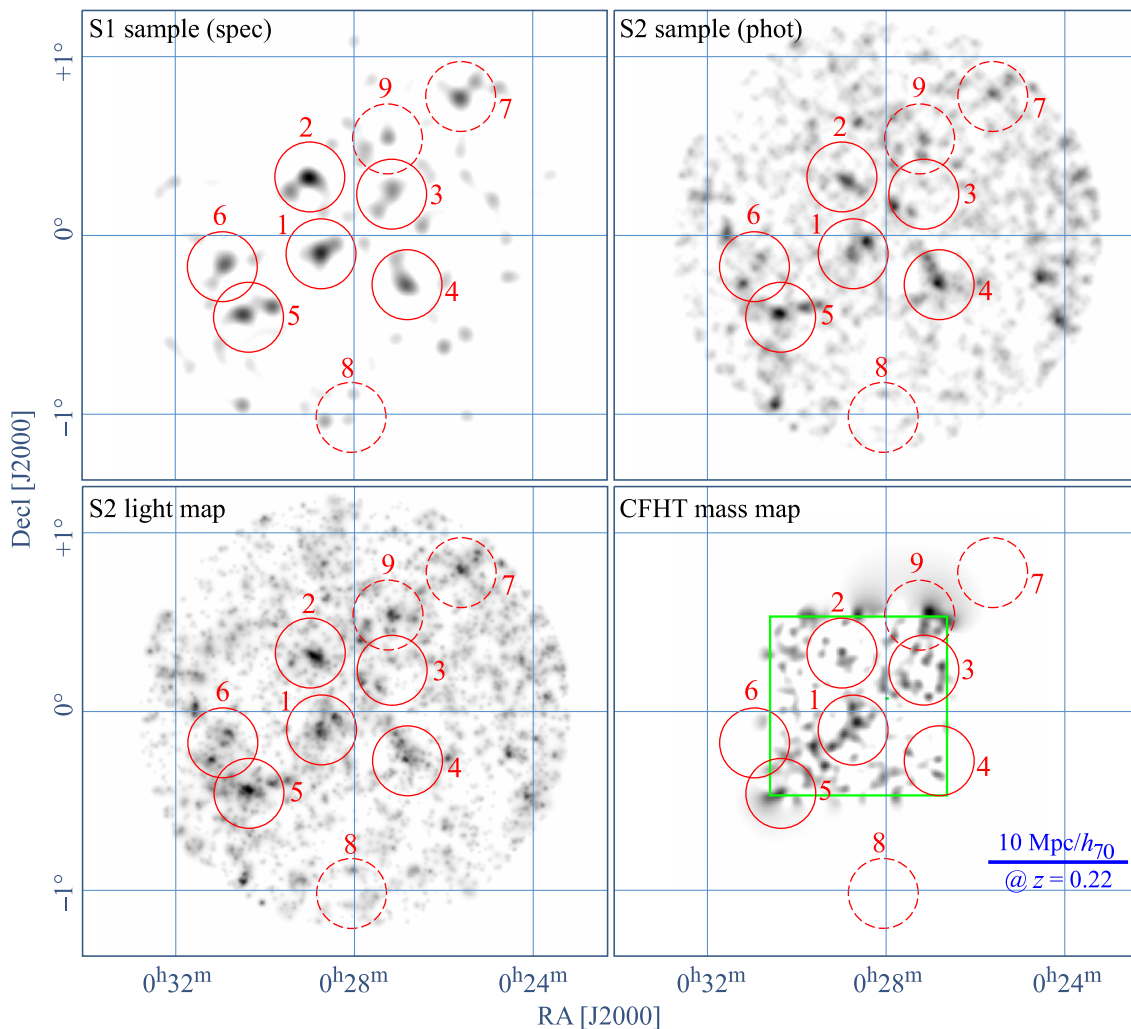
---

[3] http://terapix.iap.fr/

Figure 2. Substructures in the supercluster. Top-left: surface density map of supercluster members in the S1 (spectroscopic) sample. Top-right: surface density map of supercluster members in the S2 (photometric) sample. Bottom-left: projected light distribution of the galaxies within photometric redshift $\Delta z < 0.04$ of the supercluster mean spectroscopic redshift, $z = 0.22$. Bottom-right: weak-lensing recovered mass distribution (See Section 4 for details). The green square corresponds to the 1 deg² MegaCam/CFHT field of view. In all panels, the red circles ($R = 11.7$ arcmin) correspond to maximum projected density regions (based on the S1 sample), recentred at the location of the corresponding brightest galaxy in each maximum density box. The circles with solid lines are the substructures that will be considered in this study (see text for details).

identified in the previous maps are also present in this mass map, within the CFHT field of view (green square in the figure). This re-assures that these substructures are not projection effects, but rather actual mass concentrations. Substructure 3 is the only exception, since it is detected in redshift space, upper-left panel, but not clearly visible in any of the others. This probably means that substructure 3 is the least massive region of them all.

In Fig. 2, we can see that areas 5 and 6 overlap. After analysing the photometric redshifts of the six galaxies in the area in common, we decided to consider them as a part of group/cluster 5.

Some of those substructures might be due to projection effects and, to obtain a sample of more reliable physical structures, we have investigated their red galaxy content, since it is well know that the presence of a red sequence is conspicuous in large physical groups and clusters (e.g. Oemler 1974; Dressler 1980; Postman & Geller 1984).

We present in Fig. 3 the $(g - r)$ versus r colour–magnitude diagram for galaxies in sample S2. This figure shows a clear concentration of red galaxies. In order to make an inventory of red

objects, we have divided our sample in two using $(g - r) = 1.1$ as a cutoff based on the typical colours of galaxies at redshift $z = 0.2$ as given by Fukugita, Shimasaku & Ichikawa (1995): ellipticals $(g - r) = 1.31$, lenticulars $(g - r) = 1.13$, Sab galaxies $(g - r) = 1.01$.

The fraction of red galaxies, by this definition, is shown in Table 2 for each identified structure.

Based on this information we decided to remove substructures 7, 8 and 9 from our subsequent analysis, as they all have a fraction of red galaxies smaller than 50 per cent. We suspect that these substructures may not be bona fide bound groups and/or clusters of galaxies. We thus kept, for the present study, six groups/clusters which we considered dense and red enough to be safely considered as substructures of SC0028. Note that structure 3 appears strong in the spectroscopic redshift map (Fig. 2), while in the photometric redshift and light maps it appears diluted. We have considered this structure significant, since more than 50 per cent of its galaxies are red.

Fig. 4 presents results for the spectroscopic sample, S1. In the left-hand panel, we show the redshift distribution for each substructure.

Table 2. Structures within the supercluster: identification, coordinates, mean redshift and red fraction.

Id	α (J2000.0) (h m s)	δ (J2000.0) ($^{\circ}\ '\ ''$)	z	Fraction of red galaxies (per cent)
1	00 28 44.28	$-00\ 05\ 47.16$	0.218 ± 0.012	78
2	00 28 59.35	$+00\ 20\ 00.64$	0.222 ± 0.015	66
3	00 27 09.43	$+00\ 14\ 13.95$	0.217 ± 0.017	55
4	00 26 48.78	$-00\ 16\ 09.73$	0.226 ± 0.017	69
5^a	00 30 21.65	$-00\ 27\ 05.62$	0.225 ± 0.015	61
6^a	00 30 56.81	$-00\ 10\ 07.15$	0.225 ± 0.017	57
7	00 25 36.75	$+00\ 47\ 01.09$	0.220 ± 0.017	38
8	00 28 03.93	$-01\ 00\ 42.28$	0.217 ± 0.015	30
9	00 27 14.99	$+00\ 32\ 46.67$	0.217 ± 0.015	46
SC	00 28 00.00	$-00\ 05\ 00.00$	0.220 ± 0.001	81^b

Note^a: there is some overlap between regions 5 and 6 (Fig. 2). After checking the (photometric) redshift of the six galaxies in the overlap region we decided that this area should belong to the structure in region 5.

*Note^b*: the fraction of red galaxies was determined with the S2 sample.
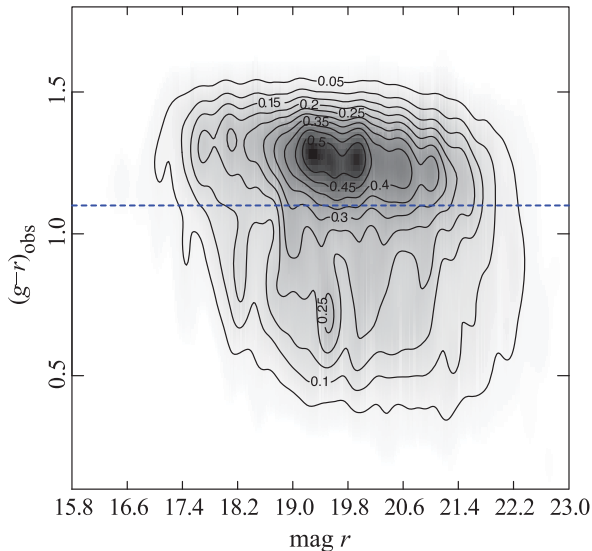
Figure 3. $g - r$ colour versus r-band magnitude diagram for the galaxies in the photometric sample S2. The continuous line at $(g - r) = 1.1$ divides the sample in red and blue galaxies (see text for details).

The dotted lines marks its mean redshift and the continuous line is the mean redshift of the supercluster.

On the middle panel we show the $(g - r) \times r$ colour–magnitude diagram of supercluster members in this sample. Dots of a given colour identify members of a specific structure. On the rightmost panel we show the distribution of the $(g - r)$ colour.

4 WEAK-LENSING ANALYSIS

In this section, we present a weak-lensing analysis of SC0028, including sample selection and the point spread function (PSF) mapping and correction. We describe the process of 2D mass reconstruction and fits to the shear profile of individual substructures. Note that the area used for the weak-lensing analysis (based on the CFHT observation) is significantly smaller than the area used for the spectroscopic and photometric analysis of the other sections, based on SDSS data (see Fig. 2).
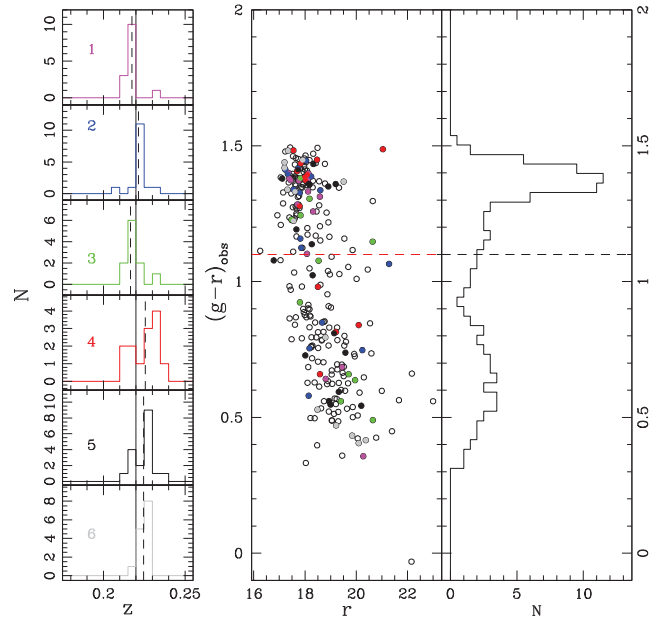
Figure 4. Results for sample S1. Left-hand panel: spectroscopic redshift distribution of each group candidate; dotted lines represent the mean redshift of the group and the continuous line is the mean redshift of the supercluster. Middle panel: the $(g - r) \times r$ colour–magnitude diagram. Each dot colour represents a structure. Black dots are galaxies in the area not associated with any structure. Right-hand panel: the $(g - r)$ distribution. The dashed horizontal line at $(g - r) = 1.1$ on the last two panels indicates our adopted separation between red and blue galaxies.

4.1 Background sample selection

The selection of the background galaxies (i.e. those affected by the gravitational lens effect) has been done by identifying the regions on a $(g - r) \times (r - i)$ colour–colour diagram where they are abundant and that have the smallest contamination by foreground and supercluster galaxies. In this section, we consider as members of the supercluster the 326 galaxies with spectroscopic redshifts with redshifts between 0.18 and 0.28. As a complement, we have also used photometric redshifts in the same interval, from the CFHTLS deep field catalogue (hereafter D; Coupon et al. 2009).

In Fig. 5 (left-hand panel), we show a $(g - r) \times (r - i)$ colour–colour diagram of the D galaxies (contours) with different colours that identify them as foreground ($z < 0.18$; blue), supercluster ($0.18 \leq z \leq 0.28$; green), and background($z > 0.28$; red). With the aid of this information we traced a triangle on this diagram, defined by vertices $(-0.11, 0.3)$, $(0.58, 1.3)$ and $(0.45, -0.16)$, that selects the regions more heavily contaminated by non-background galaxies. All the galaxies outside this selected region are our primary background galaxy sample. Using the D catalogue, we have estimated that the contamination of the background sample by field galaxies is only 0.6 per cent within the magnitude range $17 < r < 24.6$. In Fig. 5 (right-hand panel), we show the colour–colour diagram of the SC0028 field data, with the same triangular region overplotted, where the points represent the spectroscopic redshifts. Within the same magnitude limits we have, on the CFHT image, a space density of ~ 20 arcmin^{-2} candidate background galaxies.

4.2 Shape measurements

The observed shape of background galaxies is a combination of their intrinsic ellipticity, the shear caused by the lens plus distortions due
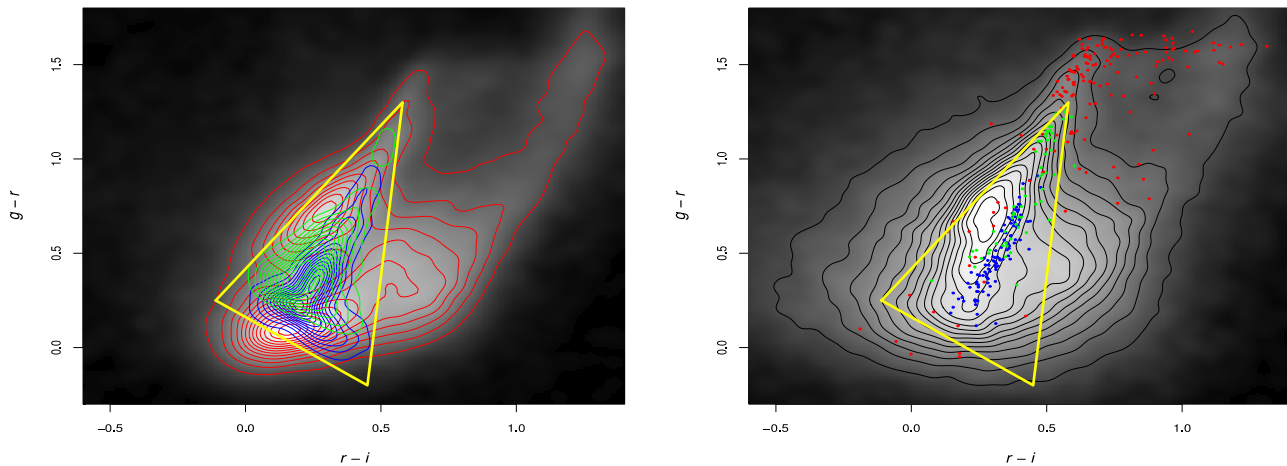
Figure 5. Left-hand panel: colour–colour diagram identifying the regions that encompasses the galaxies of D catalogue (contours) and galaxies. Supercluster galaxies ($0.18 \leq z \leq 0.28$) are in green, foreground ones ($z < 0.18$) in blue, and background galaxies ($z > 0.28$) in red. The yellow triangle encloses the region where most foreground and supercluster galaxies lie. Right-hand panel: colour–colour diagram for galaxies in the field of the supercluster SC0028 with spectroscopic redshifts (points).

to the atmosphere and the telescope+instrument optics (the PSF). The latter can be mapped through the observed shapes of stars (point sources in practice), and we can use it to deconvolve galaxy images.

We measured galaxy and PSF shapes using the IM2SHAPE software (Bridle et al. 2002), which estimates the ellipticity of astronomical objects by modelling them as a sum of Gaussians with elliptical bases. Stars are modelled as a single Gaussian whereas galaxies require a sum of two of those components, however keeping the centroid (x_c, y_c) and ellipticity (ϵ_1, ϵ_2) of both components as the same. The remaining parameters are the amplitudes (A) and a parameter related to the area of the base ellipse (ab).

We selected 1944 stars based on the FWHM (~ 0.45 arcsec) of their PSF in the range ($18 < r < 22$), where they have good signal to noise, are easily separable from galaxies, and show no signs of saturation. From this sample, we can estimate the PSF at any point of the image. We did that by smoothing the spatial variation of the relevant PSF parameters (ϵ_1, ϵ_2 and ab) with a Gaussian filter

$$\mathrm{PSF}_{\mathrm{par}} = \frac{\sum_i w_i \mathrm{PSF}_{\mathrm{par},i}}{\sum_i w_i}, \text{ with } w_i = \exp\left(\frac{-d_i^2}{2\sigma^2}\right), \quad (1)$$

where $\mathrm{PSF}_{\mathrm{par}}$ represents one of the relevant parameters at a given point of the image and d_i is the projected distance from the point to the star. The free parameter here is σ. We found a best value of 110 arcsec by minimizing the variance between predicted (interpolated) values with the actual values measured from the stars (See Fig. 6).

Next, we applied IM2SHAPE to the galaxies, tuning it to perform a PSF deconvolution using the predicted values for each galaxy position. We then excluded all the galaxies with a composed ellipticity error $\sigma_{\epsilon_1}^2 + \sigma_{\epsilon_2}^2 > 0.45$, ending up with a sample of 54 187 galaxies (~ 15 gal. arcmin^{-2}).

4.3 Mass map

We reconstruct the 2D density map from the shear information using the LENSENT2 algorithm (Bridle et al. 1998; Marshall et al. 2002), which creates a convergence (κ) map through a maximum entropy method from the ellipticity components of each background galaxy ϵ_1 and ϵ_2 and their respective uncertainties. To prevent overfitting, the resultant mass distribution is convolved with a Gaussian kernel.

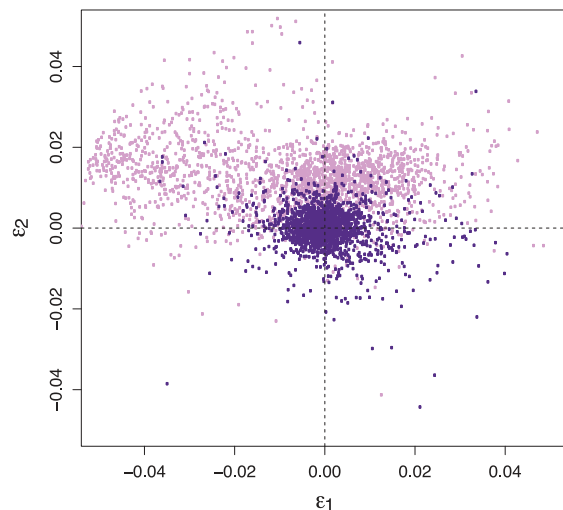**Figure 6.** Values of components of ellipticity, ϵ_1 and ϵ_2, before (pink) and after (purple) the correction described in the text, where $\langle \epsilon_1 \rangle = 10.10 \times 10^{-5}$, $\sigma_{\epsilon_1} = 7.32 \times 10^{-3}$, $\langle \epsilon_2 \rangle = 2.14 \times 10^{-5}$ and $\sigma_{\epsilon_2} = 5.21 \times 10^{-3}$.

For that we choose an scale of 150 arcsec that yields a significant result, as estimated using the Bayesian evidence, without compromising too much the spatial resolution.

The convergence is translated in to a physical mass density by multiplying it with the critical lensing surface mass density

$$\Sigma_{\mathrm{crit}} = \frac{c^2}{4\pi G} \frac{D_s}{D_l D_{ls}}, \quad (2)$$

where D_l, D_s and D_{ls} are the angular diameter distances from the observer to the lens, from the observer to the source, and from the lens to the source.

Using the photometric redshift of the deep CFHTLS catalogues, we estimated an average ratio $\langle D_s/D_{ls} \rangle$ of 1.39 (See Cypriano et al. 2004, for a description of the procedure). Therefore, we obtained $\Sigma_{\mathrm{crit}} = 3.28 \times 10^{15}$ M$_\odot$ Mpc^{-2} = 0.685 g cm^{-2}. The resultant mass distribution is shown in the lower-right panel of Fig. 2.

Table 3. Weak-lensing masses of SC0028 substructures with the CFHT imaging field.

ID	M_{200} (10^{14} M$_\odot$)
1	0.65 ± 0.40
2	2.04 ± 0.58
4	1.21 ± 0.53
5	1.82 ± 0.88

4.4 Individual masses

We determined the masses of each substructure in the supercluster by fitting NFW (Navarro, Frenk & White 1996, 1997) model predictions to their shear profiles up to a radius of 10 arcmin centred in each optically identified structure. Other values for radius have been tested, however the estimated masses remain unchanged within the statistical errors. The analytical expressions for the radial dependence of the shear of the NFW model can be seen in Wright & Brainerd (2000).

The NFW profile can be completely defined by two parameters: the mass inside a region with density 200 times the critical density, M_{200}, and a concentration parameter c. The latter is poorly constrained by our data and thus we fix it at the value of $c = 6.79$, which is appropriate for 10^{14} M$_\odot$ haloes at $z = 0.2$ (Prada et al. 2012).

We obtain the masses by minimizing the standard statistical misfit between data and model:

$$\chi^2 = \sum_i \frac{(\epsilon_{t,i} - g_{t,i})^2}{\sigma_{\text{ell}}^2 + \sigma_{m,i}^2},\tag{3}$$

where $\epsilon_{t,i}$ is the measured tangential component of the ellipticity with respect to the substructure centre for the ith galaxy and $g_{t,i}$ is the model prediction. σ_{ell} is an error related to the intrinsic ellipticity of the galaxies, for which we measured a value of $\sim$0.3, and $\sigma_{m,i}$ is associated with the measurement error of ellipticities. The latter is estimated as

$$\sigma_m = \sqrt{\frac{\sigma_{\epsilon_1}^2 + \sigma_{\epsilon_2}^2}{2}},\tag{4}$$

where σ_{ϵ_1} and σ_{ϵ_2} are the uncertainties in both components of the ellipticity estimated by IM2SHAPE in the fitting process.

In Table 3, we show the masses of the four identified substructures which are in the CFHT imaging field. The mass of region 3 is consistent with zero so it does not appear in this table. Region 6 does not appear either because its centre lies outside the CFHT image.

5 DYNAMICAL ANALYSIS

In this section, we verify if the dynamical behaviour of the substructures identified in the supercluster are consistent with the collapse scenario described in the Introduction. For this, we first determine the relative distances and peculiar velocities of these substructures. We also examine our results with a simple dynamical model.

5.1 Scaling relations: the FP

In this section, we determine the FP of early-type galaxies to obtain, in the next section, estimates of the distances to the substructures identified in the supercluster.

The FP is an empirical relation between the central velocity dispersion (σ_0), the physical effective radius (R_0) and the mean surface brightness (μ_e) within the effective radius (Terlevich et al. 1981; Djorgovski & Davis 1987; Dressler et al. 1987). The FP can be represented as

$$\log_{10}(R_0) = a \log_{10}(\sigma_0) + b \log_{10}(I_e) + c,\tag{5}$$

where I_e is the mean effective surface brightness in linear unities, $\mu_e = -2.5 \log_{10}(I_e)$.

If the FP is to be used as a distance estimator, it is convenient to adopt a direct fit for the coefficients (Bernardi et al. 2003), because it minimizes the dispersion in the physical radius R_0. Another option is by applying orthogonal fits, but this approach is more useful for the study of the global properties of elliptical galaxies or to constrain their underlying physics. Hence, we use here a direct fit for the calibration of the FP to use it as a distance indicator.

Following Bernardi et al. (2003) and Hyde & Bernardi (2009), we first renormalized the effective radii from the SDSS data (r_{sdss}) using the ratio of the minor and major galaxy semi-axes (q_{AB}) to account for the ellipticities of the galaxies in our sample.

Thus, we adopted as our galaxy radius:

$$r = r_{\text{sdss}}\sqrt{q_{\text{AB}}}.\tag{6}$$

This was done to avoid a bias due to the distribution of ellipticities (Bernardi et al. 2003).

Since the SDSS uses a fixed fibre size, the fibres cover different galaxy physical areas at different distances. Therefore, we need to take this into consideration and correct the velocity dispersion for the spectroscopic galaxies in our sample.

The aperture corrections for early-type galaxies were calculated by Jørgensen, Franx & Kjaergaard (1995) and Wegner et al. (1999) as follows:

$$\sigma_0 = \sigma_{\text{sdss}}(\frac{r_{\text{fibre}}}{r})^{0.04},\tag{7}$$

where r is the corrected radius (see above) and r_{fibre} is 1 arcsec (Ahn et al. 2012).

Finally, the surface brightness in a circle of radius r is defined as

$$\mu_0 = m + 2.5 \log_{10}(2\pi r^2),\tag{8}$$

where m is the apparent magnitude corrected by extinction and k-correction. In this work, k-corrections were calculated using the publicly available software K-CORRECT v4.2 of Blanton & Roweis (2007). The effective radius R_0 is in physical units of h_{70}^{-1} kpc.

In this subsection and in the next, we work with the S1 sample. Since we are interested here in early-type galaxies, we consider only red galaxies, those with $(g - r) > 1.1$.

We verified that the resulting sample is consistent with the morphological classification of GalaxyZoo (Lintott et al. 2011), available for 52 out of the 57 galaxies of our sample. We used for this end the assigned probabilities of being ellipticals ($P(E)$). For the 52 galaxies we found that 49 have $P(E) > 0.8$, 2 $P(E) > 0.71$ and 1 has $P(E) \sim 0.2$. Additionally, the distribution of apparent axial-ratios is consistent with that of bona fide elliptical galaxies extracted from the Third Reference Catalogue of Bright Galaxies (RC3) by G. de Vaucouleurs, A. de Vacouleurs, H.G. Corwin, R.J. Buta, P. Fouque and G. Paturel (Corwin, Buta & de Vaucouleurs 1994). We found $\sim$10 per cent of our galaxies having $(b/a) < 0.6$, where a and b are the apparent major and minor axis, similar to the RC3 sample. We conclude that our sample of galaxies should be less than 10 per cent contaminated by non-elliptical galaxies, with no impact on the FP fitting.
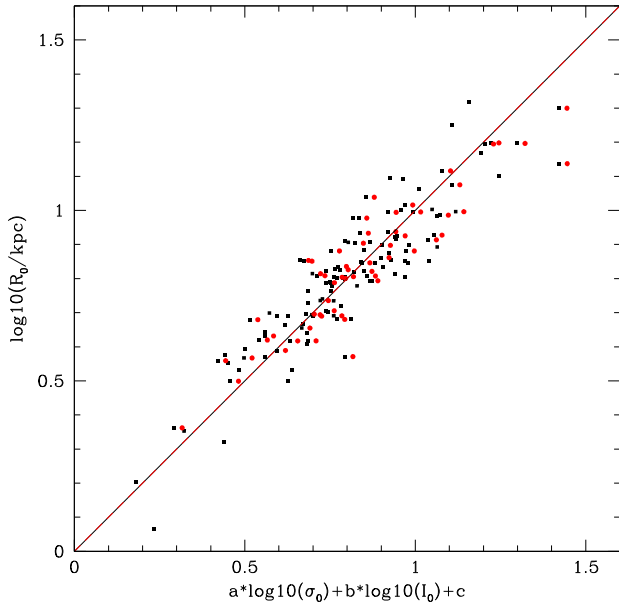
Figure 7. The FP relation. Black box symbols correspond to all red galaxies ($(g - r) > 1.1$) within $\Delta z < 0.02$ of the supercluster mean, whereas red symbols show galaxies belonging to the supercluster substructures. The dotted and dashed lines are the best linear fittings to the black and red symbols, respectively. The fittings are almost identical, making the distinction of the two lines difficult. The rms dispersions are 0.094 and 0.079 for the black and red dots, respectively.

Fig. 7 shows the best FP fit. The black box dots represent the 123 red galaxies of the spectroscopic sample with reliable central velocity dispersion measurements and within $\Delta z < 0.02$ of the mean supercluster redshift. The red dots represent 57 galaxies within the six substructures we identified. The best-fitting parameters for the whole supercluster and for galaxies in the substructures are virtually indistinguishable, with $a = 1.035 \pm 0.036$, and $b = -0.775 \pm 0.031$ and a rms scatter of 0.0941 and 0.0787 for the whole and substructure samples, respectively. These values agree well with those obtained by Saulder et al. (2013) for the SDSS-DR8.

5.2 Determination of distances and peculiar velocities

In this section, we first estimate relative distances to each substructure and, together with mean radial velocities, we estimate their peculiar radial velocities. Since we have on average only 10 galaxies in the S1 sample per substructure (see Table 4), we do not use the FP to directly measure distances to the supercluster components; instead, the zero-point offset of each substructure with respect to the overall fit can be used to find relative distances between them, keeping the coefficients a and b of equation (5) fixed. The values of the fitting coefficients are shown in Table 4, for the supercluster as a whole and for the substructures.

Following Pearson, Batiste & Batuski (2014) and Batiste & Batuski (2013), we assume that the structures are, on average, at rest with respect to the CMB. Specifically, we do not assume any peculiar motion for the supercluster centroid. Individual substructures offsets are shown in Table 4.

The error of individual galaxy distances estimated from the FP is $\Delta = \ln(10) \times rms$; since the dispersion of the FP relation is $\sim$0.079 (Table 4), Δ is around 18 per cent, in agreement with the values obtained by Pearson et al. (2014) and Batiste & Batuski (2013). For individual distances, the error percentage is reduced, assuming

Table 4. Results for the best fit of the FP for the supercluster as a whole and the substructures. Column (1) shows the identification of the structure in consideration. Column (2) presents the FP coefficients (see text for more details), with errors calculated via a bootstrapping procedure. Column (3) is the rms dispersion in the fits for the supercluster as a whole and the substructures. Column (4) gives the number of galaxies used for the FP fitting.

Sample id		rms	N
SC	$a = 1.035 \pm 0.036$	0.0787	57
	$b = -0.775 \pm 0.031$		
	$c = -9.105 \pm 0.006$		
1	$c = -9.108 \pm 0.015$	0.055	11
2	$c = -9.103 \pm 0.012$	0.061	10
3	$c = -9.098 \pm 0.014$	0.062	8
4	$c = -9.127 \pm 0.014$	0.064	9
5	$c = -9.127 \pm 0.012$	0.056	10
6	$c = -9.101 \pm 0.017$	0.065	9

Table 5. FP mean redshifts and peculiar velocities for each substructure. Column (1) gives the identification of the substructures. Column (2) gives the cluster redshift determined from the FP and Column (3) gives the derived peculiar velocity. Column (4) gives the error in the distances determined from the rms dispersion of the global fit and the number of objects in each substructure.

Id	z_{FP}	$V_p(\text{km s}^{-1})$	err(per cent)
1	0.219	−489.810	4
2	0.217	1025.577	4
3	0.215	269.444	5
4	0.228	−611.016	5
5	0.228	−815.231	4
6	0.216	2036.244	4

a Poissonian distribution, by $\Delta/\sqrt{N}$ (where N is the number of galaxies in the substructure) and is typically 6 per cent.

The comoving distances were calculated using the difference of zero-points and converted to redshift by the approximation (Peebles 1993):

$$D = \frac{cz}{H_0}\left(1 - z\frac{1+q_0}{2}\right) \approx 4283(1 - 0.225z)\,z h_{70}^{-1}\text{Mpc}, \quad (9)$$

which is appropriate at $z \sim 0.22$. We assume $q_0 = -0.55$. The peculiar velocities, v_p, were measured for each substructure using the difference between the redshift obtained with the FP (z_{FP}) and the mean spectroscopic redshift of the supercluster (z_m):

$$v_p = c\left(\frac{z_m - z_{FP}}{1 + z_{FP}}\right). \quad (10)$$

A negative velocity indicates that the substructure moves towards us, while a positive velocity indicates that it moves away from us.

A summary of the main results of this section is given in Table 5.

5.3 SC0028 as a collapsing structure

Now we test whether or not the substructures we identified are in a process of collapse towards the supercluster barycentre. The most identifiable feature of the process is a simple redshift space distortion. Substructures which are physically closer to the observer
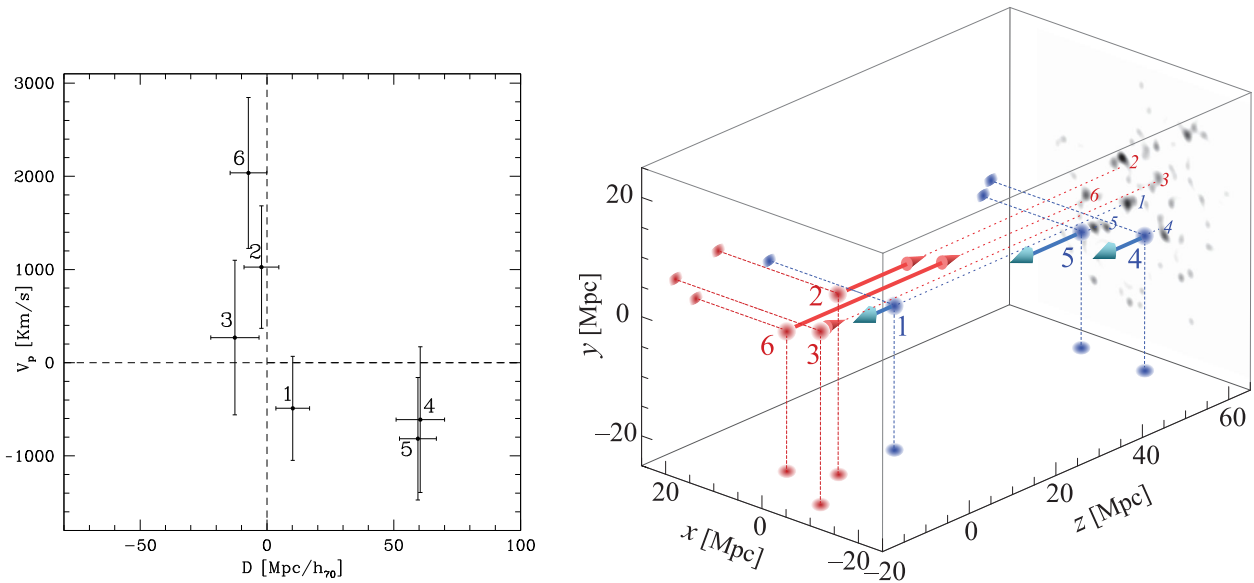
Figure 8. Left-hand panel: distances relative to the supercluster centre versus peculiar velocities for the six substructures, using the FP method. Right-hand panel: the three-dimensional spacial distribution of SC0028 substructures also showing the LOS velocity vector. The length of the V_p vectors are in arbitrary units, proportional to the velocities derived using the FP.

than the supercluster centre would feel its gravitational pull towards it, and thus will appear as having positive peculiar line-of-sight velocities (i.e. V_p points away from the observer, adding to the receding velocity.). The opposite is expected in case of substructures which are physically farther than the supercluster barycentre.

To test this hypothesis, we have used the FP distances and peculiar velocities determined in the previous subsection. The average distance of SC0028 is ~1090.50 h_{70}^{-1} Mpc so, disregarding statistical uncertainties, substructures 2, 3 and 6 would be in front of the supercluster and thus should have positive peculiar velocities, while substructures 1, 4 and 5 would be behind and are supposed to have negative peculiar velocities.

Assuming a normal distribution of probabilities for the peculiar velocities and distances, it is easy to estimate the total probability that a particular cluster/group is in one of the two expected quadrants in the $D_r \times v_p$ space, i.e. the probability of having positive peculiar velocities and negative relative distances, plus the probability of having negative peculiar velocities and positive relative distances. Assuming independence between those quantities and their errors, we find the following probabilities for each substructure be indeed in the expected quadrant where it is found: from substructure 1 to 6 we obtain, respectively, 59.4, 53.5, 53.2, 65.2, 73.2, 65.3 per cent. Combining all these p-values using the Fisher method (Hedges & Olkin 1985), we obtain a probability of 92.2 per cent. This number can be interpreted as a moderate evidence for the detection of the infall of these substructures.

Clearly most of the signal comes from substructures 4 and 5, which, in particular, presents no ambiguity regarding being on the far side of the supercluster. The overall probability is fairly insensitive to the exclusion of the less certain substructure 3.

The left-hand panel of Fig. 8 shows the phase-space D–V_p for the six substructures of SC0028. The corresponding three dimensional structure is depicted on the right-hand panel of Fig. 8, where the present collapsing state of the supercluster can be appreciated. The errors in V_p were calculated through error propagation considering the error in the distance of each substructure.

5.4 Spherical collapse model

In order to estimate the supercluster mass, we employ the spherical collapse model in an expanding universe, that describes the free-fall evolution of a shell enclosing some mass M (Gunn & Gott 1972; Lahav et al. 1991). Albeit simple, the spherical collapse model has been extensively studied and used to estimate the mass of superclusters by several authors (e.g. Dünner et al. 2006; Araya-Melo et al. 2009; Batiste & Batuski 2013; Pearson et al. 2014).

Here, we follow the time evolution of a spherical shell by solving simultaneously the motion equation (Peebles & Ratra 2003),

$$\frac{d^2r}{dt^2} + \frac{GM}{r} - H^2(z)\Omega_\Lambda r = 0, \tag{11}$$

and the background Friedman equation,

$$\frac{dz}{dt} + (1+z)H(z) = 0, \tag{12}$$

with

$$H(z) = H_0 \sqrt{\Omega_\Lambda + \Omega_M(1+z)}.$$

For each one of the six substructures, we have solved the above differential equations using, for the initial conditions, $z(0) = 0.22$, and $r(0)$ and $v_r(0)$ corresponding to each group as in Fig. 8. Note that $v_r(0)$ is always negative since the velocity vectors for all substructures point towards the centre of SC0028.

After setting the initial conditions and cosmological parameters (the standard ΛCDM model), there still one unknown in the equations since we do not know a priori the mass of the supercluster. We have searched interactively for a solution with the present observed values for $r(0)$ and $v_r(0)$ and with the smallest density contrast, $\delta_{sc} \equiv \overline{\rho}_{sc}/\rho_c$, where ρ_c is the critical density at the supercluster redshift $z = 0.22$. This yields a lower limit estimate for the supercluster mass.

We have integrated the motion equations forward and backward in time, so that we had the full trajectories from the turn-around point onwards. Fig. 9 shows these trajectories in phase-space and Table 6 summarizes the numerical integration results.
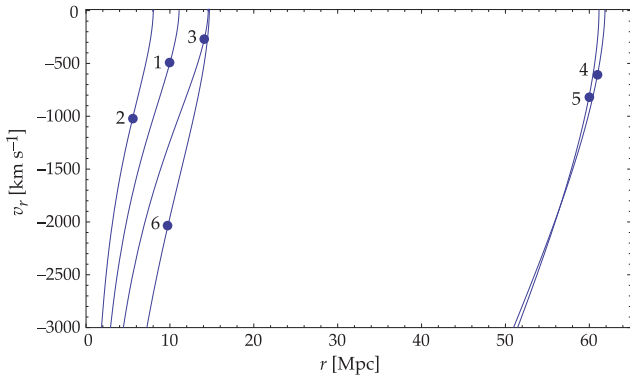
Figure 9. Free-fall trajectories for the six substructures in SC0028 in phase-space. The initial conditions are marked as large dots, with the corresponding numbers.

Table 6. Initial conditions, $r(0)$ and $v_r(0)$, and results of the integration of the spherical collapse equation. δ_{sc} is the mean density contrast of the supercluster with respect to the critical density. t_{TA} and r_{TA} are the time of turn-around and the radial distance at that time.

Obj. Id	$r(0)$ (Mpc)	$v_r(0)$ (km s^{-1})	δ_{sc}	$M[< r(0)]$ (10^{15} M$_\odot$)	t_{TA} (Gyr)	r_{TA} (Mpc)
1	10.0	−490	6.1	4.3	−5.7	11.1
2	5.5	−1026	21.6	2.6	−6.5	8.0
3	14.1	−269	3.6	7.2	−5.5	14.6
4	61.0	−611	2.8	445	−3.6	61.9
5	60.0	−815	3.2	489	−5.7	61.0
6	9.8	−2036	24.9	16.4	−7.4	14.7

Fig. 9 shows that substructures 1, 2, 3 and 6 have nearby trajectories in phase-space, while substructures 4 and 5 have very similar trajectories, but distinct from the other four. The latter pair seems to have about the same turn-around radius, compatible with an enclosing total mass of ~ 4.5–4.9×10^{17} M$_\odot$. This large mass, however, corresponds to a mean density contrast of only ~ 3 above the critical background density at $z = 0.22$.

The case of substructures 1, 2, 3 and 6 is more complex. Objects 2 and 6 suggest a high-density contrast, ~ 22–25, while objects 1 and 3 suggest a low-density contrast, in agreement with substructures 4 and 5 (between $\delta_{sc} \sim 4$ and 6). On the other hand, substructures 3 and 6 have almost the same turn-around radius, $r_{TA} \sim 14$ Mpc.

Given the uncertainties in the distance determination and our lack of information on the transverse component of the substructures peculiar velocities – we have used the line-of-sight peculiar velocity as a rough estimate of the radial peculiar velocity, v_r – we can only have an order of magnitude estimate on the supercluster mass. At a radius of 10 Mpc, the free-fall motion suggests that mass should lie between ~ 4 and 16×10^{15} M$_\odot$.

The weak-lensing masses of the individual substructures are of the order of 1–2×10^{14} M$_\odot$ (see Table 3). Within 10 Mpc from the supercluster centre, there are 3–4 of such substructures that adds up to about $\sim 3 \times 10^{14}$ (without substructure 6, which lies outside the footprint of CFHT). Therefore, most of this supercluster mass budget should be in the form of lower than $\sim 5 \times 10^{13}$ M$_\odot$ galaxy groups. That is below our detectable level with the present data.

6 SUMMARY AND CONCLUSIONS

In this work, we have analysed the gravitational dynamics of the supercluster SC0028 with spectroscopic and photometric data from SDSS-DR10. This supercluster was selected from the supercluster catalogue of Basilakos (2003), where it was classified as a filamentary structure.

We have chosen an area of 1.2 deg^2 around the supercluster and proceeded to identify substructures using density maps and red-sequence analysis. We identified nine substructures throughout the area, but three of them were discarded because their fraction of red galaxies was less than 50 per cent.

To test the collapse scenario for supercluster evolution, we have determined the distances and peculiar velocities for each substructure in the supercluster. In order to study the dynamics of these substructures, the FP was used as a distance indicator. For the spectroscopic sample, each substructure has, on average, 10 galaxies. This number is too small to determine the local FP parameters. Instead we have used the globally fitted slopes and then estimated zero-point offsets for each of the six substructures.

In order to obtain the individual distances and peculiar velocities, we considered that the supercluster's centroid does not have peculiar movements and, knowing the supercluster's distance beforehand, we computed the individual distances for each structure.

The resulting picture for SC0028 is of three substructures approaching the supercluster barycentre from the far side and three from the near side, based on the computed empirical relations with photospectroscopic data. The spatial distribution and peculiar velocities of the detected members of SC0028 support the collapsing supercluster scenario. Assuming that the dynamics may be described by a simple free-fall spherical collapse model, the overall density contrast is $\delta \sim 3$ inside a radius of 60 Mpc. In the inner region, inside 10 Mpc, the mass should be 4–16×10^{15} M$_\odot$. Most of this should be in the form of low-mass ($M \lesssim 5 \times 10^{13}$ M$_\odot$) substructures.

This work is partially based on CFHT observations (IDs 10BB07 and 10BB97) which have been processed at the TERAPIX data center located at the Institut d'Astrophisique de Paris.

REFERENCES

Ahn C. P. et al., 2012, ApJS, 203, 21
Araya-Melo P. A., Reisenberg A., Meza A., van de Weygaert R., Dünner R., Quintana H., 2009, MNRAS, 399, 97
Basilakos S., 2003, MNRAS, 344, 602
Batiste M., Batuski D. J., 2013, MNRAS, 436, 3331
Bernardi M. et al., 2003, AJ, 125, 1882
Bertin E., Arnouts S., 1996, A&AS, 117, 393
Bertin E., Mellier Y., Radovich M., Missonnier G., Didelon P., Morin B., 2002, in Bohlender D. A., Durand D., Handley T. H., eds, ASP Conf. Ser. Vol. 281, Astronomical Data Analysis Software and Systems XI. Astron. Soc. Pac., San Francisco, p. 228
Blanton M. R., Roweis S., 2007, AJ, 133, 734
Bridle S. L., Hobson M. P., Lasenby A. N., Saunders R., 1998, MNRAS, 299, 895
Bridle S., Kneib J.-P., Bardeau S., Gull S. F., 2002, in Natarajan P., ed., Proc. Yale Cosmology Workshop "The Shapes of Galaxies and Their Dark Matter Halos", Bayesian galaxy shape estimation in The Shapes of Galaxies and Their Dark Halos. World Scientific, Singapore, p. 38, available at: http://www.sarahbridle.net/im2shape/yale.pdf
Busha M. T., Adams F. C., Wechsler R. H., Evrard A. E., 2003, ApJ, 596, 713
Corwin H. G., Jr, Buta R. J., de Vaucouleurs G., 1994, AJ, 108, 2128
Costa-Duarte M. V., Sodré L., Jr, Durret F., 2011, MNRAS, 411, 1716
Coupon J. et al., 2009, A&A, 500, 981
Cypriano E. S., Sodré L. J., Kneib J.-P., Campusano L. E., 2004, ApJ, 613, 95
de Vaucouleurs G., 1953, AJ, 58, 30
Djorgovski S., Davis M., 1987, ApJ, 313, 59
Dressler A., 1980, ApJ, 236, 351
Dressler A., Lynden-Bell D., Burstein D., Davies R. L., Faber S. M., Terlevich R., Wegner G., 1987, ApJ, 313, 42
Dünner R., Araya P. A., Meza A., Reisenegger A., 2006, MNRAS, 366, 803
Dünner R., Reisenegger A., Meza A., Araya P. A., Quintana H., 2007, MNRAS, 376, 1577
Einasto J., Klypin A. A., Saar E., Shandarin S. F., 1984, MNRAS, 206, 529
Einasto M., Einasto J., Tago E., Dalton G. B., Andernach H., 1994, MNRAS, 269, 301
Einasto M. et al., 2007, A&A, 476, 697
Einasto M., Liivamägi L. J., Tago E., Saar E., Tempel E., Einasto J., Martnez V. J., Heinämäki P., 2011, A&A, 532, A5
Fukugita M., Shimasaku K., Ichikawa T., 1995, PASP 107, 945
Goto T. et al., 2002, AJ, 123, 1807
Gunn J. E., Gott J. R., III, 1972, ApJ, 176, 1
Hedges L., Olkin I., 1985, Statistical Methods for Meta-Analysis. Academic Press, San Diego
Hyde J. B., Bernardi M., 2009, MNRAS, 396, 1171
Jõeveer M., Einasto J., Tago E., 1978, MNRAS, 185, 357
Jørgensen I., Franx M., Kjaergaard P., 1995, MNRAS, 276, 1341
Lahav O., Lilje P. B., Primack J. R., Rees M. J., 1991, MNRAS, 251, 128
Lintott C. et al., 2011, MNRAS, 410, 166
Marshall P. J., Hobson M. P., Gull S. F., Bridle S. L., 2002, MNRAS, 335, 1037
Merluzzi P. et al., 2015, MNRAS, 446, 803
Nagamine K., Loeb A., 2003, New Astron., 8, 439
Navarro J. F., Frenk C. S., White S. D. M., 1996, ApJ, 462, 563
Navarro J. F., Frenk C. S., White S. D. M., 1997, ApJ, 490, 493
Neyman J., Scott E. L., Shane C. D., 1956, in Jerzy Neyman, ed.,Proceedings of the Third Berkeley Symp. on Mathematical Statistics and Probability Vol. 3, University of California Press, Berkeley, CA 75
Oemler A., Jr, 1974, ApJ, 194, 1
Pearson D. W., Batiste M., Batuski D. J., 2014, MNRAS, 441, 1601
Peebles P. J. E., 1993, Principles of Physical Cosmology. Princeton Univ. Press, Princeton, NJ
Peebles P. J. E., Ratra B., 2003, Rev. Mod. Phys., 75, 559
Postman M., Geller M. J., 1984, ApJ, 281, 95
Prada F., Klypin A. A., Cuesta A. J., Primark J., 2012, MNRAS, 423, 3018
Proust D. et al., 2006, The Messenger, 124, 30
Ragone C. J., Muriel H., Proust D., Reisenegger A., Quintana H., 2006, A&A, 445, 819
Reisenegger A., Quintana H., Carrasco E. R., Maze J., 2000, AJ, 120, 523
Rines K., Geller M. J., Diaferio A., Kurtz M. J., 2013, ApJ, 767, 15
Saulder C., Mieske S., Zeilinger W., Chilingarian I., 2013, A&A, 557, id.A21
Tago E., Einasto J., Saar E., 1984, MNRAS, 206, 559
Terlevich R., Davies R. L., Faber S. M., Burstein D., 1981, MNRAS, 196, 381
Tully R. B., Courtois H., Hoffman Y., Pomaréde D., 2014, Nature, 513, 71
Wegner G., Colless M., Saglia R. P., McMahan R. K., Davies R. L., Burstein D., Baggley G., 1999, MNRAS, 305, 259
Zucca E., Zamorani G., Scaramella R., Vettolani G., 1993, ApJ, 407, 470

This paper has been typeset from a TEX/LATEX file prepared by the author.